

# Neuroinflammation, blood-brain barrier dysfunction, and cognitive decline in pulmonary arterial hypertension: an experimental study

Received: 29 October 2025

Accepted: 9 March 2026

Published online: 03 April 2026

Cite this article as: Barbosa V.M., Santos R.T., Santos de Assumpção L. *et al.* Neuroinflammation, blood-brain barrier dysfunction, and cognitive decline in pulmonary arterial hypertension: an experimental study. *Sci Rep* (2026). <https://doi.org/10.1038/s41598-026-44104-4>

Victória Marques Barbosa, Renata Trabach Santos, Leonardo Santos de Assumpção, Aryella Maryah Couto Correa, Sabrina Sodr  Souza Serra, Louise Caroline Vitorino, Samantha Silva Christovam, Johnatas Dutra Silva, Paula Rodrigues Pereira, Nazareth Novaes Rocha, Maria Julia Cadrieskt Ribeiro, Lucas Ferreira Santos, Felipe Sim es Lemos, Patricia Rieken Macedo Rocco, Cynthia Santos Samary, Tatiana Maron-Gutierrez & Pedro Leme Silva

We are providing an unedited version of this manuscript to give early access to its findings. Before final publication, the manuscript will undergo further editing. Please note there may be errors present which affect the content, and all legal disclaimers apply.

If this paper is publishing under a Transparent Peer Review model then Peer Review reports will publish with the final article.

# **Neuroinflammation, blood-brain barrier dysfunction, and cognitive decline in pulmonary arterial hypertension: an experimental study**

**Victória Marques Barbosa<sup>1</sup>, Renata Trabach Santos<sup>1</sup>, Leonardo dos Santos de Assumpção<sup>1</sup>, Aryella Maryah Couto Correa<sup>2</sup>, Sabrina Sodr  de Souza Serra<sup>1</sup>, Louise Caroline Vitorino<sup>4</sup>, Samantha da Silva Christovam<sup>1</sup>, Johnatas Dutra Silva<sup>1</sup>, Paula Rodrigues Pereira<sup>1</sup>, Nazareth de Novaes Rocha<sup>1</sup>, Maria Julia Cadrieskt Ribeiro<sup>2</sup>, Lucas Ferreira dos Santos<sup>2</sup>, Felipe Lemos Sim es<sup>2</sup>, Patricia Rieken Macedo Rocco<sup>1</sup>, Cynthia dos Santos Samary<sup>1,3</sup>, Tatiana Maron-Gutierrez<sup>2</sup>, Pedro Leme Silva<sup>1\*</sup>**

<sup>1</sup>Laboratory of Pulmonary Investigation, Carlos Chagas Filho Institute of Biophysics, Federal University of Rio de Janeiro, Avenida Carlos Chagas Filho, s/n, Bloco G2-061, Ilha do Fund o, Rio de Janeiro 21941-902, RJ.

<sup>2</sup>Laboratory of Immunopharmacology, Oswaldo Cruz Institute, Oswaldo Cruz Foundation, Fiocruz, Rio de Janeiro, 21040-900, Brazil.

<sup>3</sup>Department of Cardiorespiratory and Musculoskeletal Physiotherapy, Federal University of Rio de Janeiro, Rio de Janeiro, 21941-599, Brazil

<sup>4</sup> Laboratory of Experimental Neuropathology, Carlos Chagas Filho Institute of Biophysics, Federal University of Rio de Janeiro, Avenida Carlos Chagas Filho, s/n, Bloco G2-061, Ilha do Fundão, Rio de Janeiro 21941-902, RJ.

\*[pedroleme@biof.ufrj.br](mailto:pedroleme@biof.ufrj.br)

## **ABSTRACT**

Pulmonary arterial hypertension is a progressive disorder characterized by elevated pulmonary vascular resistance and right ventricular hypertrophy. Beyond cardiopulmonary impairment, patients with PAH often present neuropsychological symptoms, suggesting central nervous system involvement. To explore this link, we evaluated cognitive, behavioral performance and neuroinflammatory changes during experimental PAH progression. Male Wistar rats received monocrotaline (60 mg/kg, intraperitoneally) or saline. After 14 days, motor activity, anxiety-like behavior, and recognition memory were assessed using the open field and novel object recognition tests. Hemodynamic and structural analyses confirmed increased pulmonary artery systolic pressure and right ventricular hypertrophy in PAH animals. These rats showed reduced exploratory activity and cognitive impairment, without anxiety-like behavior. Histological and immunofluorescence analyses revealed neuroinflammation in the cortex and hippocampus, with microglial and astrocytic changes and blood brain barrier disruption indicated by IgG extravasation. Elevated IL-1 $\beta$  levels were detected in the lung and plasma,

while tumor necrosis factor- $\alpha$  was increased in the hippocampus. Plasma brain natriuretic peptide levels were also elevated. Together, these findings demonstrate that experimental PAH induces early neuroinflammatory responses and cognitive dysfunction, supporting the concept that PAH extends beyond the cardiopulmonary system to affect brain structure and memory.

**Keywords:** Pulmonary arterial hypertension, Monocrotaline, Neuroinflammation, Blood-brain barrier, cognitive performance.

ARTICLE IN PRESS

## Introduction

Pulmonary arterial hypertension (PAH) is a progressive and debilitating disease characterized by pulmonary vascular inflammation and remodeling, which reduce the effective cross-sectional area of the pulmonary vasculature<sup>1</sup>. These structural changes lead to sustained increases in pulmonary vascular resistance and mean pulmonary arterial pressure ( $\geq 20$  mmHg)<sup>2</sup>. Traditionally, PAH has been regarded primarily as a cardiovascular disorder; however, emerging evidence indicates that vascular dysfunction in patients with PAH may extend systemically, potentially compromising the function of other vital organs, including the brain<sup>3,4</sup>.

Patients with PAH often exhibit reduced cerebral perfusion and impaired capillary density, as well as metabolic and muscular abnormalities, including insulin resistance, decreased skeletal muscle strength, increased protein catabolism, and mitochondrial dysfunction<sup>5</sup>. Clinically, PAH is also associated with neuropsychiatric manifestations, such as anxiety, depression, and cognitive decline, which can further impair quality of life and worsen the prognosis<sup>6</sup>. Although the mechanisms underlying cognitive impairment in PAH remain incompletely understood, neuroinflammatory processes have been proposed as potential contributors<sup>7</sup>. Specifically, excessive production of pro-inflammatory cytokines, including interleukin (IL)-1 $\beta$ , tumor necrosis factor (TNF)- $\alpha$ , and IL-6, **changes glial homeostasis**, which can exert neurotoxic effects on brain regions critical for cognition and

anxiety regulation<sup>8,9</sup>.

Understanding the mechanisms underlying brain dysfunction during PAH development is essential. Early recognition may inform risk factor management, slow cognitive decline, and improve adherence to therapy. We hypothesized that pulmonary vascular injury in PAH extends to the central nervous system (CNS), promoting neuroinflammatory changes that contribute to cognitive impairment and anxiety-like behavior. In this study, we investigate anxiety-like behavior, cognitive performance, and neuroinflammatory markers during the development of experimental PAH.

## **Results**

### **Heart**

On day 15, PASP was higher in the PAH group compared with the CTRL group ( $65 \pm 17$  mmHg versus  $30 \pm 9$  mmHg;  $p < 0.001$ ) (Fig. 1A). The PAT/PET ratio was reduced in the PAH group, confirming the presence of pulmonary hypertension ( $0.28 \pm 0.03$  versus  $0.43 \pm 0.05$ ;  $p < 0.001$ ) (Fig. 1B). In addition, the RVH index was increased in the PAH group ( $0.29 \pm 0.07$  versus  $0.20 \pm 0.02$ ;  $p = 0.001$ ) (Fig. 1E). LVEF was similar in the PAH and CTRL animals ( $84\% \pm 5\%$  versus  $82\% \pm 5\%$ ,  $p = 0.385$ ), which suggests adequate distal organ perfusion (Fig. 1D).

### **Lungs**

Histologic analysis revealed early vascular remodeling in PAH animals. Perivascular collagen deposition was increased ( $34\% \pm 7\%$  versus  $19\% \pm$

3%;  $p = 0.001$ ) (Fig. 2A, B), and arteriolar wall thickness was greater in PAH animals compared with CTRL animals ( $59\% \pm 5\%$  versus  $49\% \pm 7\%$ ;  $p = 0.006$ ) (Fig. 3C, D).

### **Motor and cognitive functions**

Rotarod testing showed no differences in latency to fall between the groups ( $175 \pm 90$  s versus  $195 \pm 91$  s;  $p = 0.614$ ), indicating intact motor function (Fig. 3A). During the open field test, PAH animals exhibited reduced total distance traveled compared with controls ( $23 \pm 7$  m versus  $36 \pm 9$  m;  $p = 0.0008$ ), reflecting decreased exploratory activity (Fig. 3B). This reduction was observed in both peripheral and ( $2.3 \pm 1.3$  m versus  $3.8 \pm 1.2$  m;  $p = 0.010$ ) central ( $29.0 \pm 5.7$  m versus  $31.8 \pm 8.2$  m;  $p = 0.010$ ) zones (Fig. 3E, F). **No differences were observed in the center/periphery distance ratio between the CTRL and PAH groups ( $0.113 \pm 0.356$  vs.  $0.107 \pm 0.595$ ;  $p = 0.408$ ) (Fig. 3G).** Total distance traveled correlated negatively with PASP ( $r = -0.47$ ;  $p = 0.021$ ) (Fig. 3I). No differences were detected in the number of entries into the center ( $15 \pm 7$  versus  $19 \pm 7$ ;  $p = 0.163$ ) or time spent in the center ( $28 \pm 12$  s versus  $28 \pm 13$  s;  $p = 0.937$ ), suggesting no anxiety-like behavior at this stage (Fig. 3C, D). **Figure 3H shows representative track plots from one animal per group recorded during the 10-min test session.** During the NOR test, CTRL animals spent significantly more time exploring the novel object than the familiar one ( $69.2\%$  versus  $30.8\%$ ;  $p < 0.001$ ), indicating intact recognition memory. In contrast, PAH rats displayed no preference between novel and familiar objects ( $52.7\%$  versus  $47.3\%$ ;  $p =$

0.263), consistent with impaired short-term recognition memory (Fig. 4).

### **Neuroinflammation**

Immunolabeling for Iba-1 revealed an increased number of microglia in PAH animals in both the motor cortex ( $37 \pm 2$  versus  $21 \pm 1$  cells/mm<sup>2</sup>;  $p < 0.001$ ) and hippocampus ( $17.6 \pm 0.5$  versus  $9.4 \pm 3.0$  cells/mm<sup>2</sup>;  $p < 0.001$ ) (Figs. 5A and 5B). The area of the microglial cells was also larger in PAH rats ( $75 \pm 1$   $\mu\text{m}^2$  versus  $63 \pm 3$   $\mu\text{m}^2$ ;  $p < 0.001$ ), indicating morphological changes consistent with activation (Figs. 5C and 5D). Figure 5E illustrate one representative figure for immunolabeling for Iba-1 in cortex and hippocampus in both groups. GFAP-positive astrocytes were more numerous in PAH animals compared with controls in the cortex ( $20 \pm 4$  versus  $11 \pm 3$  cells/ $\mu\text{m}^2$ ;  $p < 0.001$ ) and hippocampus ( $31 \pm 5$  versus  $20 \pm 2$  cells/ $\mu\text{m}^2$ ;  $p < 0.001$ ) (Figs. 6A and 6B). Astrocyte hypertrophy was also evident; the mean cell area was larger in PAH animals (cortex:  $15 \pm 4$   $\mu\text{m}^2$  versus  $6 \pm 1$   $\mu\text{m}^2$ ; hippocampus:  $145 \pm 31$   $\mu\text{m}^2$  versus  $88 \pm 8$   $\mu\text{m}^2$ ;  $p < 0.001$ ) (Figs. 6C and 6D). Figure 6E illustrate one representative figure for GFAP in cortex and hippocampus in both groups.

### **Sholl Analysis**

Sholl analysis revealed significant morphological differences in astrocytes from both the cortex and hippocampus between CTRL and PAH groups. In the cortex, astrocytes from PAH animals exhibited a significantly higher number of intersections at radial distances of 10  $\mu\text{m}$  and 15  $\mu\text{m}$  from the soma compared to CTRL ( $p = 0.003$  for both distances). In addition, analysis

of the maximum radius demonstrated a significant increase in overall astrocytic ramification in the PAH group in the cortex ( $p = 0.009$ ). In the hippocampus, astrocytes from PAH animals also displayed increased morphological complexity, with a significantly higher number of intersections observed at 15  $\mu\text{m}$  and 20  $\mu\text{m}$  from the soma ( $p = 0.001$  for both distances). Consistently, the maximum radius was significantly greater in the PAH group compared to CTRL ( $p = 0.028$ ), indicating an overall enlargement of the astrocytic arbor in this region.

The analysis of microglial cells revealed no significant morphological differences between CTRL and PAH groups in the cortex across the analyzed radial distances. Consistently, the maximum Sholl radius did not differ between groups in this region ( $p = 0.924$ ). In the hippocampus, microglial morphology was comparable between groups, with no significant differences observed at most radial distances. A modest difference was detected at 15  $\mu\text{m}$  from the soma, while the maximum Sholl radius remained unchanged between CTRL and PAH groups ( $p = 0.160$ ), indicating no overall alteration in microglial arbor size in this region.

### **NeuN+ cells**

In the cortex, neuronal counts were similar between groups (CTRL:  $187 \pm 35$  cells/ $\mu\text{m}^2$  vs. PAH:  $175 \pm 51$  cells/ $\mu\text{m}^2$ ;  $p = 0.642$ ) (Figures 8A and 8C), indicating preserved neuronal density in this region. In the hippocampus the PAH group exhibited a marked reduction in NeuN+ cells compared with controls (CTRL:  $98 \pm 28$  cells/ $\mu\text{m}^2$  vs. PAH:  $66 \pm 5$  cells/ $\mu\text{m}^2$ ;  $p = 0.019$ )

(Figures 8B and 8D), which depicts neuronal loss.

### **BBB permeability**

Blood-brain barrier (BBB) integrity was assessed by quantification of cortical extravascular IgG immunoreactivity. The PAH group exhibited a significant increase in IgG leakage compared with controls (CTRL:  $3.95 \pm 1.16$  a.u./ $\mu\text{m}^2$  vs. PAH:  $8.62 \pm 4.71$  a.u./ $\mu\text{m}^2$ ;  $p = 0.0022$ ), indicating enhanced vascular permeability in the PAH model (Fig. 9).

### **Astrocyte-vessel interaction and feet coverage**

Representative confocal images revealed qualitative differences in astrocyte-vessel interaction between the experimental groups (Fig. 10). In CTRL animals, GFAP+ astrocytes exhibited a more regular morphology, with well-defined processes closely associated with the vascular wall. In contrast, in PAH group, astrocytes showed an apparent increase in GFAP immunoreactivity, accompanied by hypertrophic cell bodies, thicker and more branched processes around blood vessels. This pattern suggests greater astrocytic reactivity and remodeling of the astrocytic-vascular interface.

### **ELISA Essay**

Plasma BNP levels were increased in PAH animals compared with controls (median, interquartile range [IQR]: 163 [95–386] pg/ $\mu\text{L}$  versus 45 [29–46] pg/ $\mu\text{L}$ ];  $p < 0.001$ ). BNP concentrations in the lung and hippocampus did not differ between the groups; cortical BNP was reduced in PAH animals (0.68

[0.48–0.92] pg/mg versus 6.14 [4.12–15.45] pg/mg;  $p < 0.001$ ) (Fig. 11A). TNF levels were similar in plasma, lung, and cortex between the groups but were increased in the hippocampus of PAH animals (median [IQR]: 74 [38–94] pg/mg versus 23 [13–47] pg/mg;  $p = 0.022$ ), indicating local inflammatory activation (Fig. 11B). IL-1 $\beta$  was increased in the lung (189 [184–235] pg/mg versus 110 [105–130] pg/mg;  $p = 0.004$ ) and plasma (66 [60–91] pg/ $\mu$ L versus 48 [38–55] pg/ $\mu$ L;  $p = 0.028$ ) of PAH animals; cortical and hippocampal IL-1 $\beta$  levels remained unchanged (Fig. 11C).

## Discussion

In this experimental model of monocrotaline-induced pulmonary arterial hypertension, our study identified several key findings: (1) early-stage PAH was associated with reduced exploratory locomotor activity and cognitive impairment, without motor deficits or anxiety-like behavior; (2) these behavioral alterations coincided with neuroinflammation in the cortex and hippocampus, characterized by region-specific morphological remodeling and increased numbers of microglia and astrocytes; (3) elevated hippocampal TNF expression and increased systemic IL-1 $\beta$  levels in plasma and lungs indicated the involvement of both central and peripheral inflammatory pathways; and (4) evidence of blood–brain barrier disruption suggested vascular dysfunction as a potential contributor to neuroinflammation. **Importantly, (5) quantitative Sholl analysis revealed a selective increase in astrocytic branching complexity and process extension in cognitively relevant brain regions, highlighting astrocytes as key cellular**

mediators of PAH-associated neuroinflammatory remodeling and (6) neuronal analysis indicated alterations in neuronal integrity within the hippocampus, a region critically involved in memory processing, suggesting that glial and vascular changes may converge to impact neuronal function and contribute to cognitive deficits observed in early PAH.

PAH is increasingly recognized as a systemic disorder affecting multiple organs beyond the cardiopulmonary system. Clinical studies report renal dysfunction, skeletal muscle impairment, altered angiogenesis, and neuropsychiatric symptoms including cognitive deficits, depression, and anxiety, all of which contribute to reduced quality of life <sup>5,6</sup>. These findings underscore the need to investigate CNS involvement in PAH and to identify strategies that prevent or mitigate neurological and emotional consequences.

The MCT model is well established for inducing PAH in rodents. Following metabolic activation to monocrotaline pyrrole (MCTP), the compound selectively injures pulmonary endothelial cells, promoting inflammation and vascular remodeling. It has been shown that MCT can be administered by subcutaneous and intraperitoneal routes <sup>10</sup>. We have chosen intraperitoneal MCT route due to the following reasons: 1) faster absorption into the systemic circulation via the portal system; 2) it may induce subacute model with shorter survival period; 3) the area of drug reaction of intraperitoneal cavity is larger than a subcutaneous MCT injection and other routes of administration <sup>11</sup>. Therefore, the plasma concentration is increased after

intraperitoneal MCT absorption within a short time, and the toxic effect and inflammation may be more severe. Although MCTP circulates systemically, its toxicity largely spares other organs, including the brain, likely due to selective molecular targets such as the extracellular calcium-sensing receptor<sup>12,13</sup>. By using a moderate dose (50–60 mg/kg), this study minimized off-target toxicity, allowing CNS alterations to be attributed primarily to pulmonary vascular injury rather than direct neurotoxicity.

Unlike studies examining later disease stages, the present work focused on early PAH (two weeks), before severe cardiac dysfunction could confound behavioral testing. Motor performance in the rotarod test remained preserved, confirming that reduced exploratory activity in the open field test reflected behavioral rather than motor impairment. Anxiety-like behavior was not detected, while cognitive dysfunction was evident in the novel object recognition test, consistent with early deficits in short-term memory. Similar behavioral impairments have been reported in models of heart failure with preserved ejection fraction, in which systemic inflammation contribute to cognitive decline.<sup>14</sup>

Our study indicates region-specific astrocytic morphological alterations in the present experimental PAH, characterized by changes in branching patterns and process extension in both cortical and hippocampal astrocytes. In the cortex, astrocytes from PAH animals exhibited increased branching complexity together with an enlarged maximum radius, suggesting an expansion of astrocytic arbors. In the hippocampus, astrocytes also showed

increased structural complexity and greater overall process extension. Together, these findings support the presence of astrocytic structural remodeling in PAH across distinct brain regions. It is known that astrocytes play a central role at the neurovascular unit, where they regulate BBB integrity, vascular tone, and bidirectional communication between the peripheral circulation and the central nervous system.<sup>15</sup> The observed increase in astrocytic process complexity and territorial expansion may reflect an adaptive response to systemic inflammatory cues associated with PAH, potentially aiming to preserve vascular stability and neural homeostasis. However, sustained astrocytic hypertrophy has also been linked to altered synaptic modulation, impaired glutamate clearance, and dysregulated neurovascular coupling, which could contribute to cognitive and behavioral deficits.<sup>16,17</sup>

In contrast to astrocytes, microglial morphology did not show marked alterations in either the cortex or hippocampus at the 14-day time point of the PAH model. Sholl analysis and maximum radius measurements did not reveal clear morphological differences between groups. However, an increase in mean microglial cell size and cell number was observed in the PAH group, suggesting the presence of subtle microglial alterations. Microglial responses to inflammatory stimuli are dynamic and depend on disease stage therefore; the absence of pronounced morphological remodeling at 14 days does not exclude microglial involvement in PAH. Consistent with previous experimental PAH studies, neuroinflammation can

be inferred from increased microglial number and changes in microglial profiles without requiring a classical amoeboid transformation as a mandatory indicator of reactivity. Together, our findings suggest that, at this time point, microglia exhibit an early or intermediate reactive phenotype that may precede more substantial structural changes at later stages of PAH progression, when sustained systemic inflammation becomes more prominent.<sup>18</sup> Together, these findings suggest that astrocytic reactivity is an early and prominent cellular response in the PAH brain, while pronounced microglial morphological changes may occur preferentially with prolonged or advanced disease progression.

Endothelial dysfunction is a hallmark of PAH and likely contributes to BBB impairment, permitting peripheral cytokines to enter the brain and affect glial cells.<sup>19</sup> Elevated hippocampal TNF coincided with glial reactivity, while IL-1 $\beta$  levels were increased in the lungs and plasma but not yet in the brain, suggesting that peripheral cytokines may indirectly drive neuroinflammation through humoral or neural pathways<sup>20,21</sup>. Longitudinal studies are warranted to determine whether IL-1 $\beta$  later accumulates in specific brain regions and how these processes evolve over time.

BNP levels were increased in plasma, reflecting cardiovascular stress, but decreased in the cortex and unchanged in the hippocampus. Given BNP's neuroprotective and anti-inflammatory roles in the CNS, reduced cortical BNP may represent an early loss of neuroprotection, consistent with findings in neurodegenerative conditions<sup>22,23</sup>. These regional differences

highlight the complex neurohumoral regulation occurring during early PAH. Strengths of this study include the evaluation at an early disease stage, which allowed dissociation of CNS changes from severe cardiac dysfunction, and the integration of behavioral, histological, and biochemical analyses to reveal mechanistic links between pulmonary and neural inflammation. Limitations include the absence of autonomic nervous system assessment, lack of glycocalyx analysis, and the cross-sectional design, which precludes evaluation of temporal progression, **absence of anxiety-specific tests which may have precluded the difference between PAH and CTRL animals in the present study.**

In summary, these findings provide new insights into the systemic nature of PAH and its early impact on the CNS. The observation that neuroinflammation and cognitive impairment occur before overt cardiac dysfunction suggests that brain alterations may develop insidiously in patients, contributing to reduced quality of life and treatment adherence. Identifying early biomarkers of neuroinflammation, such as hippocampal TNF elevation and BBB disruption, may guide clinical monitoring and therapeutic interventions. Together, these data support the inclusion of cognitive and neuroimaging assessments in the evaluation of PAH and provide a rationale for the development of neuroprotective and anti-inflammatory strategies aimed at improving neurological and clinical outcomes.

## **Conclusion**

MCT-induced PAH in rats leads to early cognitive impairment and reduced exploratory activity, accompanied by neuroinflammation in the cortex and hippocampus. These alterations occur in the absence of motor deficits or anxiety-like behavior and are associated with region-specific changes in TNF and BNP expression, increased systemic IL-1 $\beta$ , and BBB disruption. Our findings highlight that PAH is a systemic disease with significant CNS involvement and underscore the importance of monitoring and potentially targeting neuroinflammatory pathways to mitigate cognitive decline in PAH.

## **Methods**

### Study approval

The experimental protocol was approved by the Institutional Animal Care and Use Committee of the Health Sciences Centre at the Federal University of Rio de Janeiro (CEUA 082/22). All animals were housed and treated in accordance with the “Principles of Laboratory Animal Care” established by the National Society for Medical Research and the Guide for the Care and Use of Laboratory Animals (U.S. National Academy of Sciences). This study adhered to the ARRIVE guidelines <sup>24</sup>. Animals were maintained under a controlled temperature (23 °C) with a 12-hour h light/dark cycle and had ad libitum access to food and water ad libitum.

### **Animal preparation and experimental protocol**

Twenty-four male Wistar rats (CEMIB, UNICAMP, São Paulo; 160–200 g, 7

weeks old) were randomly assigned to two experimental groups: control (CTRL, saline, n = 10) and pulmonary arterial hypertension (PAH, monocrotaline [MCT], 60 mg/kg, n = 14; C2401, Sigma-Aldrich, St. Louis, MO, USA). PAH was induced on day 0 by a single intraperitoneal injection of monocrotaline, while control animals received an equivalent volume of saline. This route of administration was chosen to ensure rapid and homogeneous systemic delivery, as described in previous studies using monocrotaline<sup>25</sup>. Two weeks after PAH induction (day 14), animals underwent behavioral assessments, beginning with the rotarod test, followed by the open field test and the novel object recognition test. On the following day (day 15), transthoracic echocardiography was performed to evaluate cardiac structure and function. Immediately after echocardiographic assessment, animals were euthanized and plasma, brain, lung and heart were collected for subsequent biochemical, histological, and molecular analyses.

### **Behavioral Assessments**

Motor coordination and balance were evaluated using the Rotarod test. Rats were placed on an accelerating rotating rod (4-40 rpm) after a 2-minute habituation for 2 min. The latency to fall was recorded to rule out motor deficits<sup>26</sup>. The Open Field Test (OFT) assessed anxiety-like behavior in a 60 × 60 × 60 cm arena. Rats explored freely for 10 min, and total distance, center versus periphery activity, and time spent in the center were measured. Reduced center exploration indicated anxiety-like behavior.<sup>27</sup>

Learning and memory were assessed using the Novel Object Recognition (NOR) test in the same arena. The test consisted of a training phase in which animals were allowed to freely explore two identical objects for 10 minutes. After a 2-hour inter-trial interval, animals were returned to the arena for a 10-minute test phase, during which one familiar object and one novel object were presented. Time spent exploring familiar versus novel objects was recorded and analyzed as a percentage with a 50% chance level. All analyses were performed by investigators blinded to the experimental groups.<sup>28,29</sup>

### **Echocardiography**

On day 15, transthoracic echocardiography was performed under 2% isoflurane anesthesia (Cristália, Brazil) using a UGEO HM70A system (Samsung, Brazil) with an 8-13 MHz linear probe. Pulmonary artery systolic pressure (PASP) was estimated using  $PASP = 137.2 - 3.3 \times \text{pulmonary arterial acceleration time (PAT)}$ . Left ventricular ejection fraction (LVEF), PAT, and ejection time (PET) were measured, and PAT/PET ratios were calculated as an indirect index of PAH.<sup>30-32</sup> Measurements followed the American Society of Echocardiography and European Association of Cardiovascular Imaging guidelines.<sup>33</sup>

Right ventricular hypertrophy was assessed using the Fulton index, calculated as the ratio of right ventricle weight (RV) to the combined weight of the left ventricle and septum (LV + S), normalized to body weight.<sup>34</sup>

### **Histology**

Immediately after echocardiography, animals were heparinized, anesthetized with midazolam (2 mg/kg, intraperitoneal) and ketamine (75 mg/kg, intraperitoneal), and euthanized by exsanguination. Hearts, lungs, and brains were collected for histological and protein analyses. All histological evaluations were performed by investigators blinded to group allocation.

The left lung was fixed in 10% neutral-buffered formalin under 3 cmH<sub>2</sub>O positive end-expiratory pressure (PEEP) to preserve parenchymal architecture. Paraffin-embedded sections (4 μm) were stained with Masson's trichrome to evaluate perivascular collagen deposition. Collagen accumulation around terminal arterioles (<150 μm in diameter) was quantified in ten randomly selected fields per slide using QuPath (v0.5.0) and ImagePro Plus (v4.5.1).<sup>35</sup>

### **Smooth Muscle Actin Immunohistochemistry.**

Lung sections underwent antigen retrieval followed by α-smooth muscle actin (α-SMA) immunostaining. Ten arteriolar fields (<150 μm) per section were analyzed to determine pulmonary vascular wall thickness, calculated as: PWT (%) = 100 × (1 - A<sub>int</sub>/A<sub>ext</sub>), where A<sub>int</sub> correspond to the luminal and external areas defined by the internal and external elastic laminae, respectively.<sup>35</sup>

### **Brain Immunofluorescence**

Brains were dissected, fixed in 4% paraformaldehyde for 24 h, and cryoprotected in graded sucrose solutions (10%, 20%, and 30%; 24 h each).

Tissues were embedded in OCT compound (Sakura, USA), and coronal sections (10  $\mu$ m) were obtained using a cryostat (Leica CM1850, Germany). Sections were mounted on silanized slides (Dako, USA) and stored at  $-20^{\circ}\text{C}$  until processing.

For immunofluorescence, tissue sections were washed three times in phosphate-buffered saline containing 0.1% Tween-20 (PBS-T) for 5 min each and incubated overnight at  $4^{\circ}\text{C}$  with primary antibodies diluted in blocking solution: anti-Iba1 (1:300, Wako, Denmark), anti-GFAP (1:1000, Sigma-Aldrich, USA), and anti-NeuN (1:500, Merck Millipore, USA). After three additional PBS-T washes, sections were incubated for 2 h at room temperature with the appropriate secondary antibodies: goat anti-rabbit Alexa Fluor 488 (1:400, Life Technologies, USA) for Iba1 and NeuN, and goat anti-rabbit Alexa Fluor 546 (1:500, Life Technologies, USA) for GFAP. Sections were then washed, counterstained with DAPI (1:700, Invitrogen, USA) for 15 min, and mounted using Vectashield antifade mounting medium (Vector Laboratories, USA). For astrocyte-vascular analysis, tissue sections were incubated overnight at  $4^{\circ}\text{C}$  with anti-GFAP (1:1000, Sigma-Aldrich, USA), followed by goat anti-rabbit Alexa Fluor 488 secondary antibody (1:400, Life Technologies, USA). Vascular structures were labeled using a directly conjugated conjugated Alexa Fluor 568 anti-CD31/Pecam-1 (Cell Signaling; #61255) Sections were counterstained with DAPI and mounted using Vectashield Mounting Media (Sigma, F6057).

Images from the hippocampus and motor cortex were acquired at  $20\times$

magnification using a confocal microscope (Zeiss, Germany). Iba1-, GFAP-, and NeuN-positive cells were quantified within predefined regions of interest. Six animals per group were included in the analyses. For each animal, two brain sections were analyzed, and two non-overlapping fields per section were acquired from anatomically standardized regions of the cortex and hippocampus (CA1 region and dentate gyrus). Values obtained from all fields and sections were averaged to generate a single value per animal, which was used as the experimental unit for all statistical analyses.

### **Sholl Analysis**

Sholl analysis was performed to evaluate cellular process complexity. Briefly, images were acquired using confocal microscopy Nikon C2 (Nikon, USA) and analyzed using Fiji/ImageJ software (NIH, USA) with the Neuroanatomy plugin. Concentric circles centered on the soma were generated at fixed radial intervals, and the number of intersections between cellular processes and each circle was quantified. From this analysis, the total number of intersections was obtained as a measure of branching complexity. In addition, the total radius, defined as the maximum distance reached by cellular processes from the soma, was measured and used as an indicator of overall process length and spatial extension. All analyses were performed under identical parameters for all experimental groups, and the researcher was blinded to group allocation.

### **BBB integrity**

BBB integrity was evaluated by immunofluorescence detection of

endogenous IgG in brain sections. Sections were incubated with Alexa Fluor 488 conjugated anti-rat IgG and counterstained with DAPI, then mounted with Vectashield. Fluorescence images were acquired using a Zeiss fluorescence microscope. IgG extravasation into the cortical parenchyma was semi-quantitatively assessed as a marker of BBB disruption. Mean fluorescence intensity of parenchymal IgG was quantified using ImageJ, with intravascular signal excluded by threshold-based segmentation. Quantified values were averaged per animal and normalized to control values for statistical analysis.<sup>36</sup>

### **Molecular biology**

Right lung, plasma, cortex, and hippocampus were snap-frozen and stored at  $-80^{\circ}\text{C}$ . Tissues were homogenized in appropriate lysis buffers, and protein levels were quantified via the Bradford assay. TNF- $\alpha$ , IL-1 $\beta$ , and brain natriuretic peptide (BNP) concentrations were measured using commercial ELISA kits, following the manufacturer's protocols (PeproTech, USA; Elabscience, China). All analyses were performed by investigators blinded to the group allocation.

### **Statistical analysis**

Normality of the data was assessed by the Shapiro-Wilk test. Parametric or non-parametric tests (Student's t test or Mann-Whitney test) were applied as appropriate. Correlations between total distance traveled and PASP were assessed using Spearman's test. Analyses were performed in GraphPad Prism v9.02. Data are presented as means  $\pm$  standard deviation or median

(interquartile range).

## References

1. Humbert, M. *et al.* Advances in Therapeutic Interventions for Patients With Pulmonary Arterial Hypertension. *Circulation* **130**, 2189–2208 (2014).
2. Galiè, N., McLaughlin, V. V., Rubin, L. J. & Simonneau, G. An overview of the 6th World Symposium on Pulmonary Hypertension. *Eur Respir J* **53**, 1802148 (2019).
3. Kurakula, K. *et al.* Endothelial Dysfunction in Pulmonary Hypertension: Cause or Consequence? *Biomedicines* **9**, 57 (2021).
4. Malenfant, S. *et al.* Compromised Cerebrovascular Regulation and Cerebral Oxygenation in Pulmonary Arterial Hypertension. *JAMA* **6**, e006126 (2017).
5. Nickel, N. P. *et al.* Beyond the Lungs: Systemic Manifestations of Pulmonary Arterial Hypertension. *Am J Respir Crit Care Med* **201**, 148–157 (2020).
6. White, J., Hopkins, R. O., Glissmeyer, E. W., Kitterman, N. & Elliott, C. G. Cognitive, emotional, and quality of life outcomes in patients with pulmonary arterial hypertension. *Respir Res* **7**, 55 (2006).
7. Hilzendege, A. M., Shenoy, V., Raizada, M. K. & Katovich, M. J. Neuroinflammation in Pulmonary Hypertension: Concept, Facts, and Relevance. *Curr Hypertens Rep* **16**, 469 (2014).
8. Smith, J. A., Das, A., Ray, S. K. & Banik, N. L. Role of pro-inflammatory cytokines released from microglia in neurodegenerative diseases. *Brain Research Bulletin* **87**, 10–20 (2012).
9. Yirmiya, R. & Goshen, I. Immune modulation of learning, memory, neural plasticity and neurogenesis. *Brain, Behavior, and Immunity* **25**, 181–213 (2011).
10. Zhuang, W. *et al.* Pulmonary arterial hypertension induced by a novel method: Twice-intraperitoneal injection of monocrotaline. *Exp Biol Med (Maywood)* **243**, 995–1003 (2018).
11. Flessner, M. F., Lofthouse, J. & Zakaria, E. R. Improving Contact Area between the Peritoneum and Intraperitoneal Therapeutic Solutions. *Journal of the American Society of Nephrology* **12**, 807–813 (2001).
12. Lachant, D. J. *et al.* Low dose monocrotaline causes a selective pulmonary vascular lesion in male and female pneumonectomized rats. *Experimental Lung Research* **44**, 51–61 (2018).
13. Gomez-Arroyo, J. G. *et al.* The monocrotaline model of pulmonary hypertension in perspective. *American Journal of Physiology-Lung Cellular and Molecular Physiology* **302**, L363–L369 (2012).
14. Patil, S. *et al.* Microglial metabolic reprogramming drives cognitive decline in heart failure with preserved ejection fraction. Preprint at <https://doi.org/10.1101/2025.09.10.675257> (2025).
15. Linnerbauer, M., Wheeler, M. A. & Quintana, F. J. Astrocyte Crosstalk in CNS Inflammation. *Neuron* **108**, 608–622 (2020).
16. Ortega, A. *et al.* ASTROGLIA: Molecular Mechanisms, Functional Roles, and Neurophysiological Implications in the Central Nervous System. *Life* **15**, 1505 (2025).
17. Lawal, O., Ulloa Severino, F. P. & Eroglu, C. The role of astrocyte structural plasticity in regulating neural circuit function and behavior. *Glia* **70**, 1467–1483 (2022).

18. Sharma, R. K. *et al.* Involvement of Neuroinflammation in the Pathogenesis of Monocrotaline-Induced Pulmonary Hypertension. *Hypertension* **71**, 1156–1163 (2018).
19. Müller, L. & Di Benedetto, S. Neuroimmune crosstalk in chronic neuroinflammation: microglial interactions and immune modulation. *Front. Cell. Neurosci.* **19**, 1575022 (2025).
20. Vitkovic, L. *et al.* Cytokine signals propagate through the brain. *Mol Psychiatry* **5**, 604–615 (2000).
21. Barbosa-Silva, M. C. *et al.* Infectious disease-associated encephalopathies. *Crit Care* **25**, 236 (2021).
22. Hodes, A. & Lichtstein, D. Natriuretic Hormones in Brain Function. *Front. Endocrinol.* **5**, (2014).
23. Mahinrad, S. *et al.* Natriuretic Peptides in Post-mortem Brain Tissue and Cerebrospinal Fluid of Non-demented Humans and Alzheimer's Disease Patients. *Front. Neurosci.* **12**, 864 (2018).
24. Percie Du Sert, N. *et al.* The ARRIVE guidelines 2.0: Updated guidelines for reporting animal research. *PLoS Biol* **18**, e3000410 (2020).
25. Zhang, H. *et al.* Protective effect of hydrogen sulfide on monocrotaline-induced pulmonary arterial hypertension via inhibition of the endothelial mesenchymal transition. *Int J Mol Med* <https://doi.org/10.3892/ijmm.2019.4359> doi:10.3892/ijmm.2019.4359.
26. Shan, H.-M., Maurer, M. A. & Schwab, M. E. Four-parameter analysis in modified Rotarod test for detecting minor motor deficits in mice. *BMC Biol* **21**, 177 (2023).
27. Prut, L. & Belzung, C. The open field as a paradigm to measure the effects of drugs on anxiety-like behaviors: a review. *European Journal of Pharmacology* **463**, 3–33 (2003).
28. Kanatsou, S. & Krugers, H. Object-context Recognition Memory Test for Mice. *BIO-PROTOCOL* **6**, (2016).
29. Lueptow, L. M. Novel Object Recognition Test for the Investigation of Learning and Memory in Mice. *JoVE* 55718 (2017) doi:10.3791/55718.
30. Jones, J. E. *et al.* Serial noninvasive assessment of progressive pulmonary hypertension in a rat model. *American Journal of Physiology-Heart and Circulatory Physiology* **283**, H364–H371 (2002).
31. Thibault, H. B. *et al.* Noninvasive Assessment of Murine Pulmonary Arterial Pressure: Validation and Application to Models of Pulmonary Hypertension. *Circ: Cardiovascular Imaging* **3**, 157–163 (2010).
32. Trittmann, J. K. *et al.* PATET ratio by Doppler echocardiography: noninvasive detection of pediatric pulmonary arterial hypertension. *Pediatr Res* **92**, 631–636 (2022).
33. Lang, R. M. *et al.* Recommendations for Cardiac Chamber Quantification by Echocardiography in Adults: An Update from the American Society of Echocardiography and the European Association of Cardiovascular Imaging. *Journal of the American Society of Echocardiography* **28**, 1–39.e14 (2015).
34. JoVE Video Dataset.
35. Braga, C. L. *et al.* Therapeutic effects of hypoxia-preconditioned bone marrow-derived mesenchymal stromal cells and their extracellular vesicles in experimental pulmonary arterial hypertension. *Life Sciences* **329**, 121988 (2023).
36. Hiles-Murison, B. *et al.* Blood-brain barrier disruption and ventricular enlargement are the earliest neuropathological changes in rats with repeated sub-

concussive impacts over 2 weeks. *Sci Rep* **11**, 9261 (2021).

### Figures Legends

Fig. 1. Echocardiographic parameters. A) Pulmonary Artery Systolic Pressure. B) PAT/PET ratio. PAT: pulmonary acceleration time; PET: pulmonary ejection time. C) Echocardiographic representative images, yellow outline, peak blood flow in the pulmonary artery. D) Left ventricular ejection fraction. E) Right ventricular hypertrophy index calculated as the ratio of the right ventricular weight to the combined weight of the left ventricle and septum (RV/LV + S), adjusted for body weight. CTRL: control; PAH: pulmonary arterial hypertension. Data are presented as means  $\pm$  SD. Comparisons made using the Unpaired t test ( $p < 0.05$ ).

Fig. 2. A) Percentage of perivascular collagen deposition. B) Representative images of perivascular collagen in pulmonary arteries (in blue). C) Quantification of vessel wall thickness. D) Representative immunohistochemistry images of  $\alpha$ -smooth muscle actin (in brown). Data are presented as means  $\pm$  SD. Comparisons made using the Unpaired t test ( $p < 0.05$ ).

Fig. 3. A) Rotarod Test. Latency to fall (seconds). B) Open field test. Total distance traveled (meters) C) Center entries D) Center time in seconds E)

Center distance (meters) F) Periphery distance (meters) G) Ratio center/periphery. H) Representative track plot reports recorded during the 10 min test sessions. I) Correlation between PASP and total distance traveled was assessed using Spearman's correlation. A negative correlation was observed ( $r = -0.467$ ,  $p = 0.021$ ). CTRL: control. PAH: pulmonary arterial hypertension. Data are presented as means  $\pm$  SD. Comparisons made using the Unpaired t test ( $p < 0.05$ ).

Fig. 4. Novel object recognition test. Time in percentage exploring familiar or new objects. CTRL: control. PAH: pulmonary arterial hypertension. The results were expressed as the percentage of time exploring each object and analyzed according to the mean exploration time for each object with the fixed value of 50% (chance level). Data are presented as means  $\pm$  SD. Comparisons made using the Unpaired t test ( $p < 0.05$ ).

Fig. 5: Immunofluorescence of microglia (Iba-1+) in cortex (A and B) and hippocampus (C and D) at D15 at 20 $\times$  magnification. A) Number of Iba-1+ cells in cortex; B) Mean microglial area in cortex; C) Number of Iba-1+ cells in hippocampus; D) Mean microglial area in hippocampus. E) Representative images obtained of DAPI and Iba-1+, only Iba-1+, and only Iba-1+ enlarged. Scale bar: 100  $\mu$ m. Enlarged images obtained at 100 $\times$  magnification. Scale bar: 20  $\mu$ m. CTRL: control; PAH: pulmonary arterial hypertension. Data are presented as mean  $\pm$  SD, with individual data points representing

independent animals. Comparisons made using the Unpaired t test ( $p < 0.05$ ).

Fig. 6: Immunofluorescence of astrocytes (GFAP+) in cortex (A and B) and hippocampus (C and D) at D15 at 20× magnification. A) Number of GFAP+ cells in cortex; B) Mean microglial area in cortex; C) Number of GFAP+ cells in hippocampus; D) Mean microglial area in hippocampus. E) Representative images obtained of DAPI and GFAP+, only GFAP+, and only GFAP+ enlarged. Scale bar: 100  $\mu\text{m}$ . Enlarged images obtained at 100x magnification. Scale bar: 20  $\mu\text{m}$ . CTRL: control; PAH: pulmonary arterial hypertension. Data are presented as mean  $\pm$  SD, with individual data points representing independent animals. Comparisons made using the Unpaired t test ( $p < 0.05$ ).

Fig. 7. (A-D) Sholl analysis showing the number of intersections as a function of radial distance from the soma in cortical astrocytes. (A) Cortical astrocytes (B) CA1 astrocytes (C) microglial cortex (D) microglial hippocampus from control (CTRL) and pulmonary arterial hypertension (PAH) groups. (E-H) Quantification of maximum Sholl radius, reflecting total process extension, revealed a significant increase in cortical (E) and CA1 (F) astrocytes from the PAH group, while no differences were observed in cortical (G) or CA1 microglia (H). Data are presented as mean  $\pm$  SD, with individual data points representing single cells. Comparisons were performed using two-way ANOVA followed by Tukey multiple comparisons

for Sholl profiles and Mann-Whitney tests for maximum radius comparisons ( $p < 0.05$ ).

Fig. 8. (A-B) Representative immunofluorescence images of NeuN-positive neurons (green) and DAPI nuclear staining (blue) in the cortex (A) and hippocampus (B) of control (CTRL) and pulmonary arterial hypertension (PAH) groups. (C-D) Quantification of NeuN-positive cells in the cortex (C) and hippocampus (D). No significant difference in neuronal density was observed in the cortex between CTRL and PAH groups. In contrast, a significant reduction in NeuN-positive cells was detected in the hippocampus of PAH animals compared to CTRL ( $p = 0.019$ ). Data are presented as mean  $\pm$  SD, with individual data points representing independent animals. Comparisons made using the Unpaired t test ( $p < 0.05$ ).

Fig. 9. (A) Representative immunofluorescence images showing extravascular IgG immunofluorescence (green) in the cortex of control (CTRL) and pulmonary arterial hypertension (PAH) animals, indicating blood brain barrier (BBB) leakage. Scale bar: 100  $\mu$ m. (B) Quantitative analysis of IgG fluorescence intensity outside blood vessels revealed a significant increase in the PAH group compared to controls. Data are presented as median and interquartile range (Q1-Q3), with individual data points representing independent animals. Comparisons were performed by Mann-Whitney test ( $p < 0.05$ ).

Fig 10. Representative immunofluorescence images of CTRL and PAH groups showing individual fluorescence channels at 60× magnification. Scale bar: 20 μm. Nuclei are labeled with DAPI (blue), astrocytes with GFAP (green), and vascular structures with CD31/PECAM-1 (red). Images illustrate the distribution of each marker in the cortex. Merged images illustrate the spatial relationship between astrocytic processes and blood vessels in CTRL and PAH animals.

Fig. 11. Quantification of BNP, TNF-α, and IL-1β in lung, plasma, cortex, and hippocampus measured by ELISA. Data are presented as median with interquartile range (Q1-Q3). Comparisons were performed using the Unpaired t test or Mann-Whitney test ( $p < 0.05$ ).

### **Data availability**

The datasets used and/or analyzed during the current study available from the corresponding author on reasonable request.

### **Funding**

This work received funding from the Carlos Chagas Filho Foundation for Research Support of the State of Rio de Janeiro (FAPERJ, E-26/202.766/2018, E-26/010.001488/2019).

### **Acknowledgements**

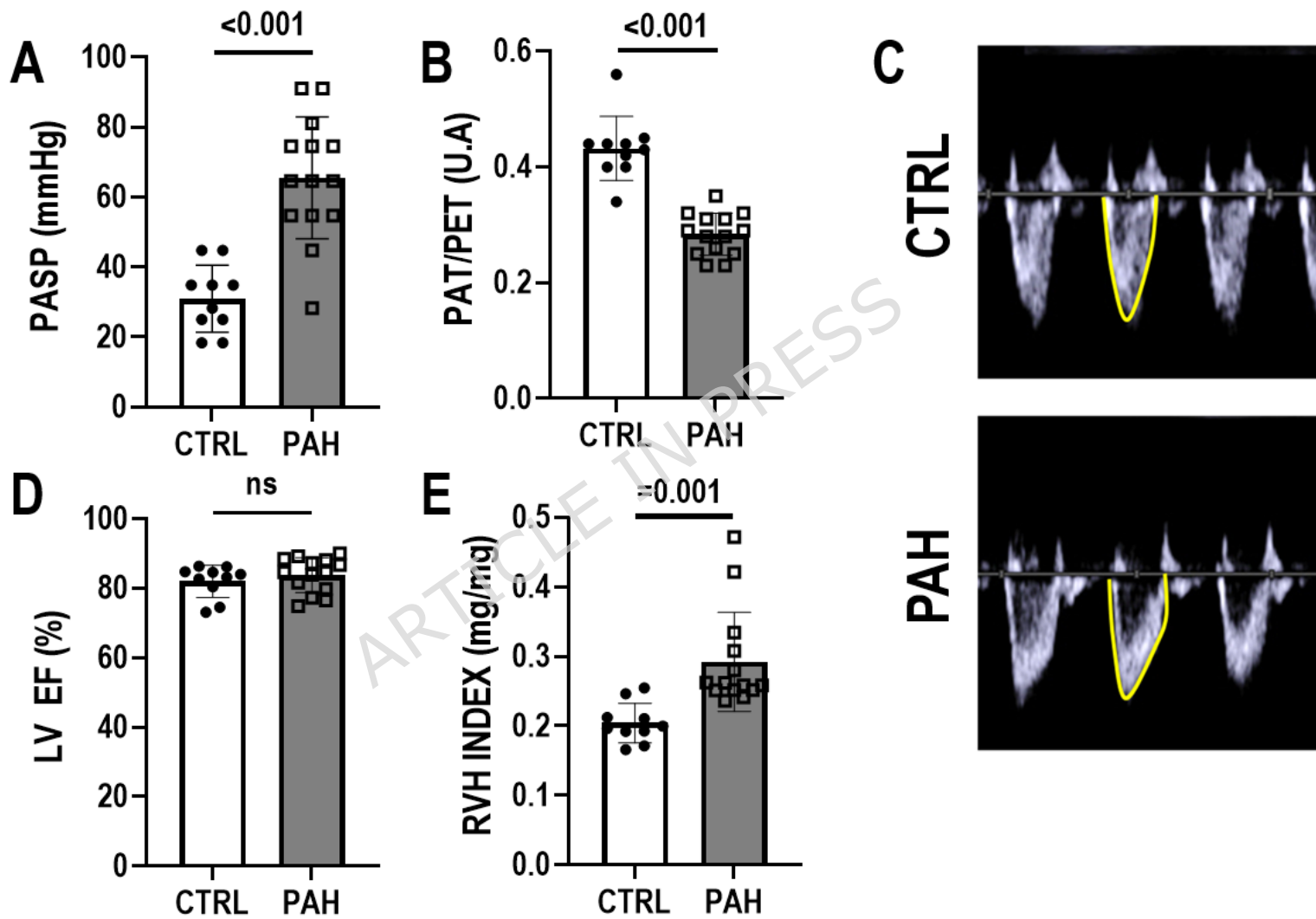
The authors thank Mr. André Benedito da Silva for support with the

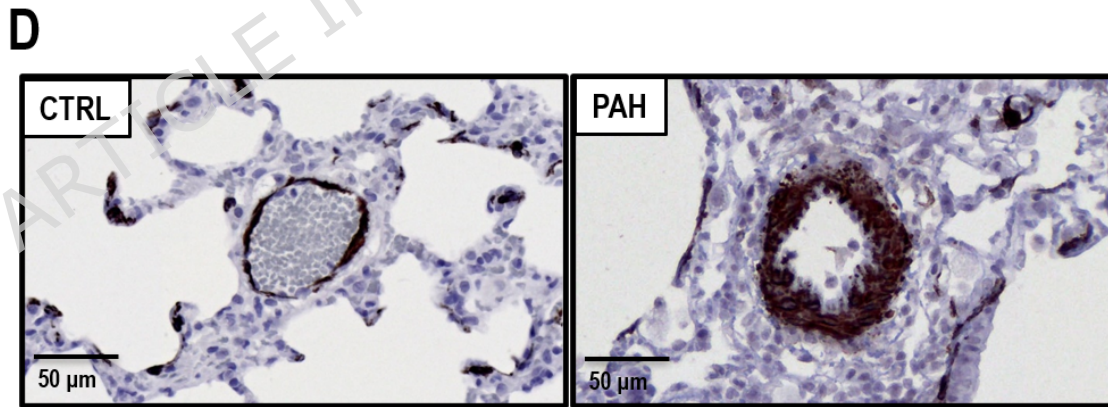
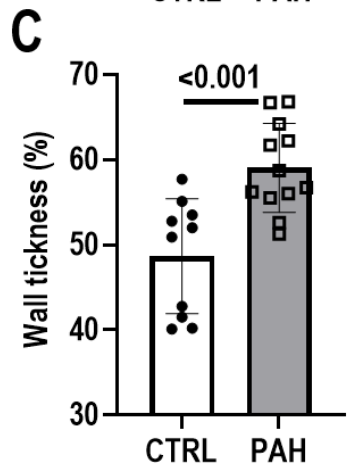
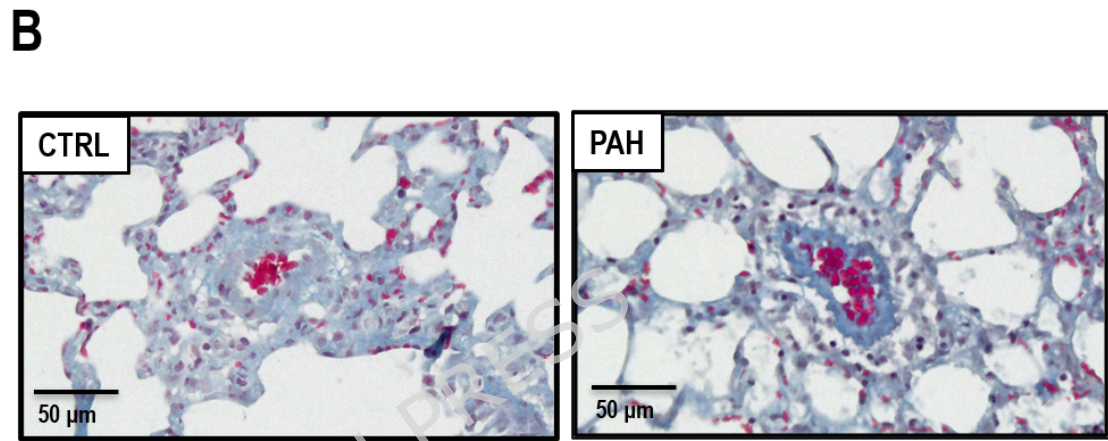
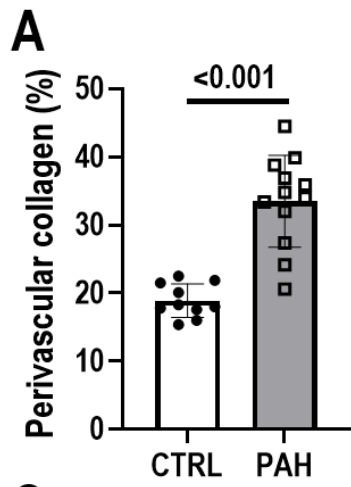
experiments and Ms Verônica Cristina dos Santos Lima for animal care, and Ms. Lorna O'Brien for English grammar revision. The authors declare that they have not use AI-generated work in this manuscript.

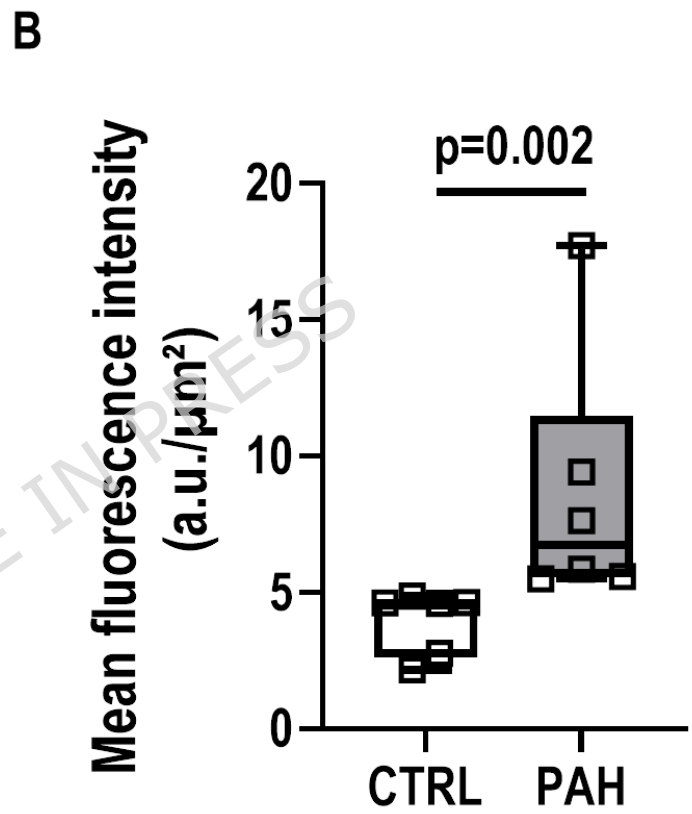
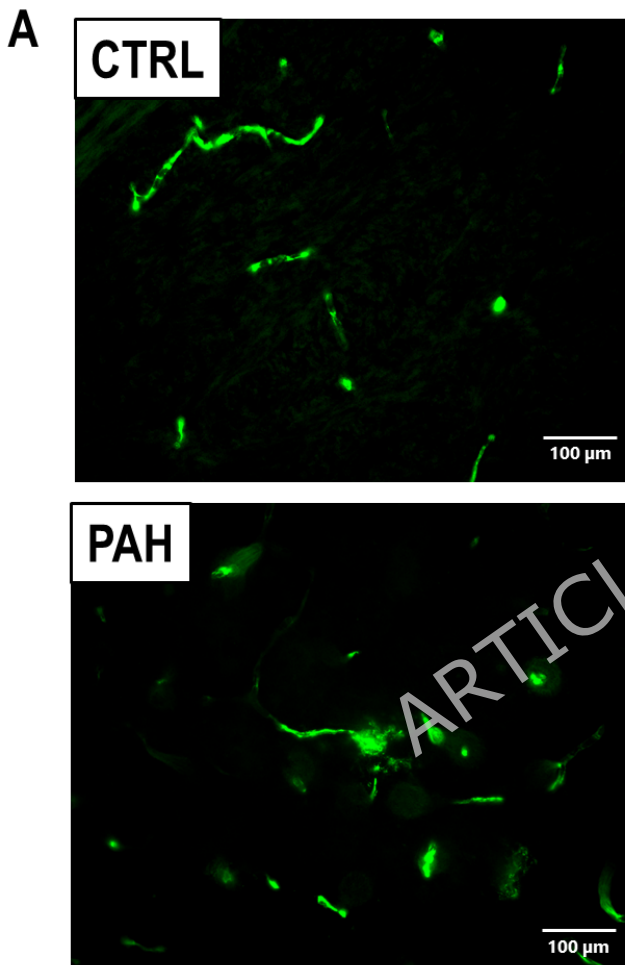
**Author contributions statement**

VMB, RTS, CSS, TMG, and PLS were involved in the conception and design of the study. VMB, RTS, LSA, AMCC, JDS, SSC, NNR, MJCR, LCV, LFS, FLS, and PLS were involved in the acquisition of data. VMB, RTS, NNR, TMG, and PLS were involved in analyzing the results. All authors reviewed the manuscript.

ARTICLE IN PRESS

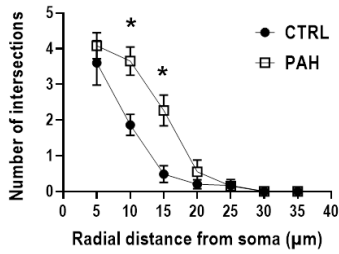
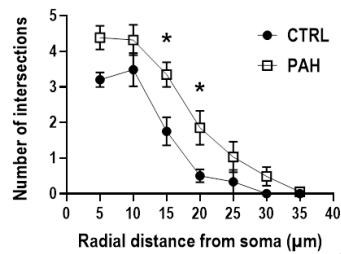
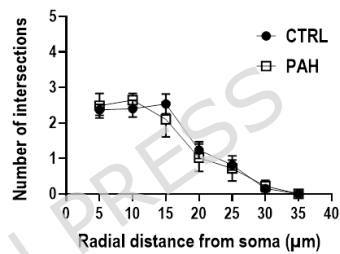
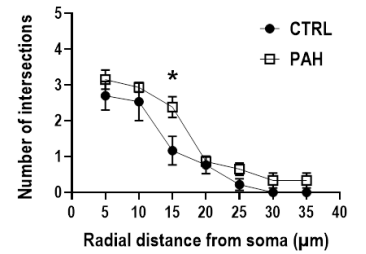
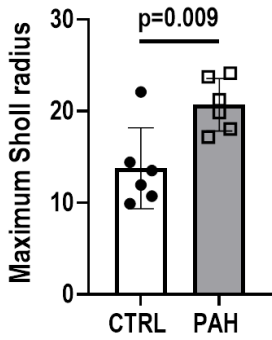
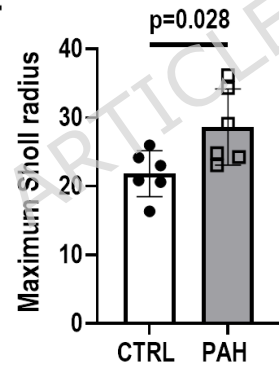
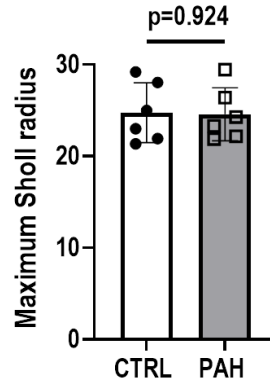
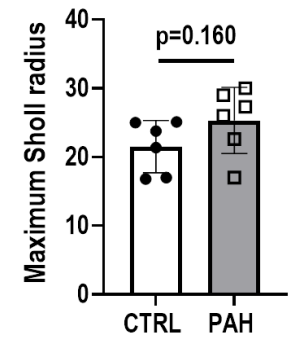


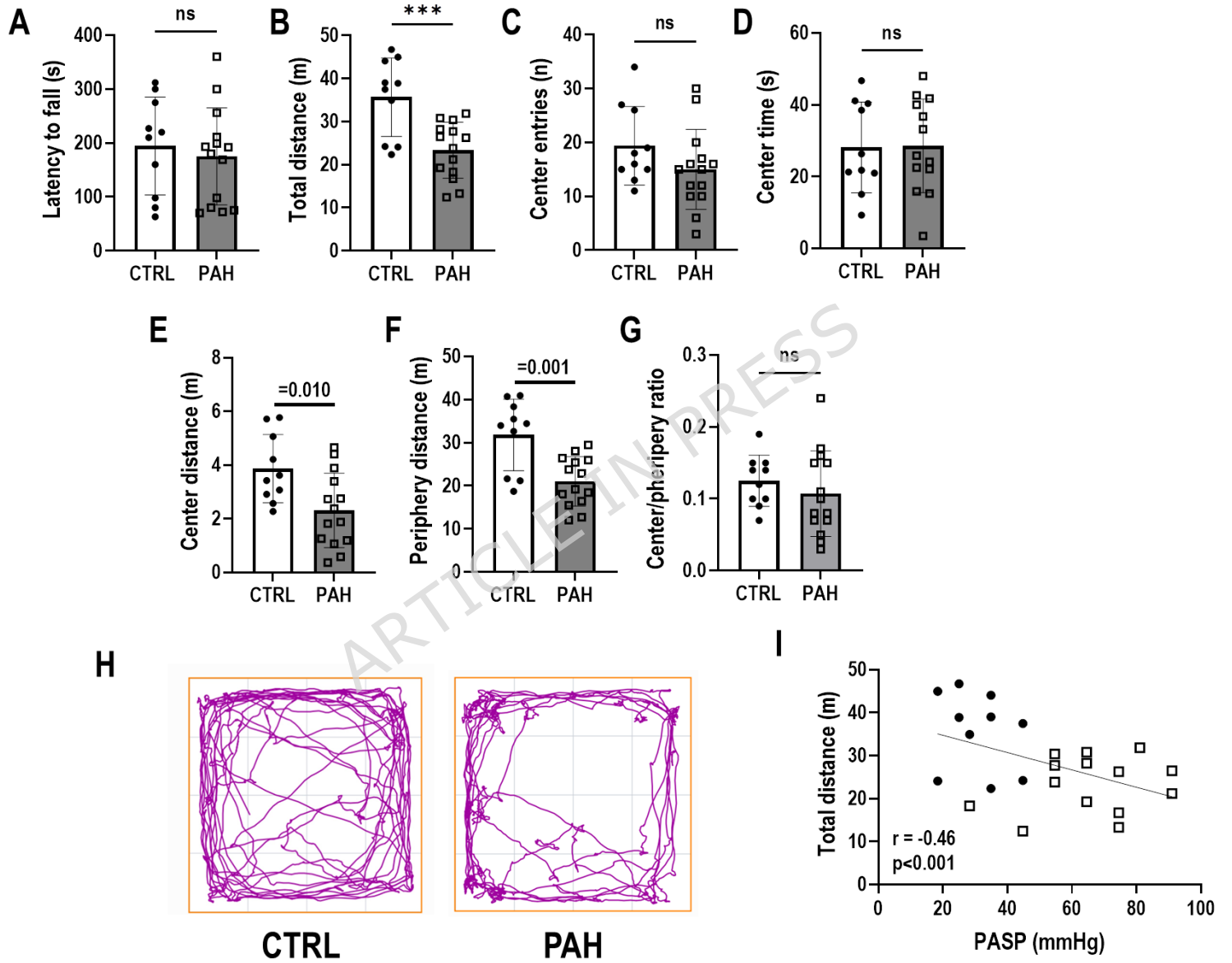


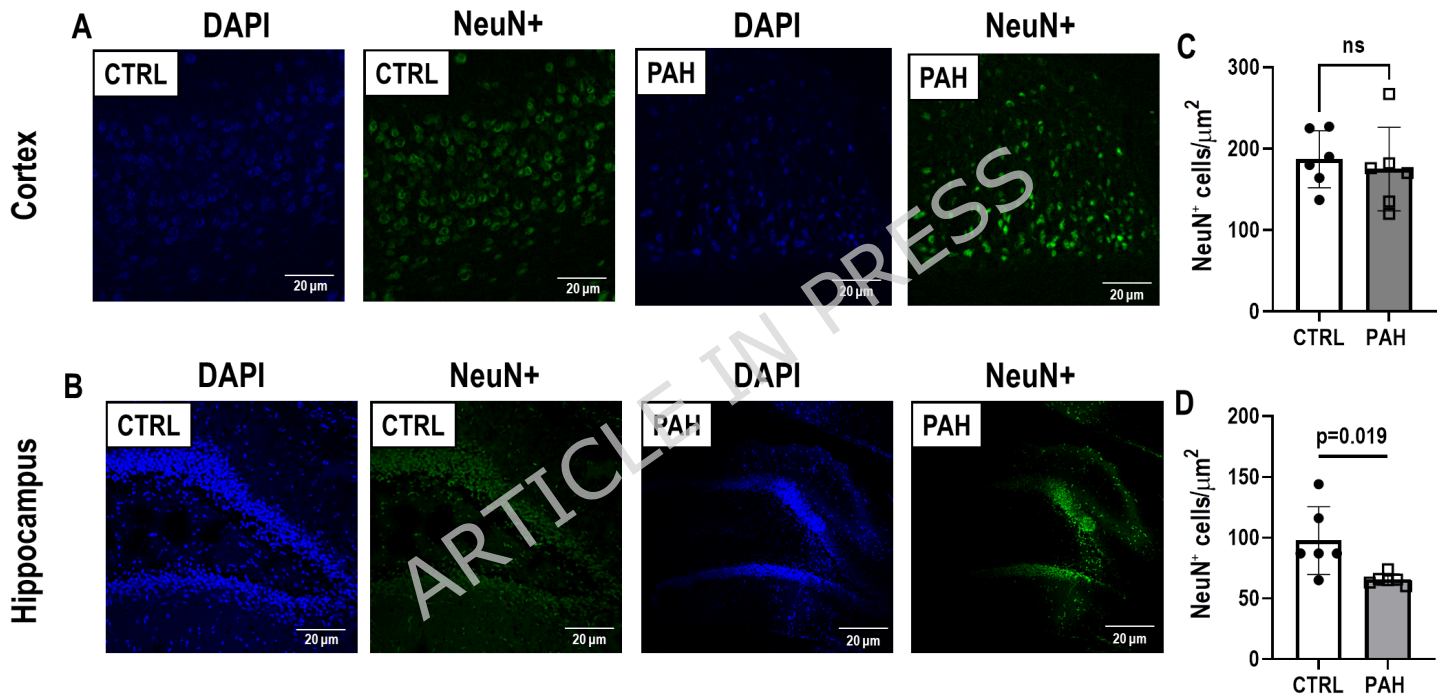


## Astrocytes

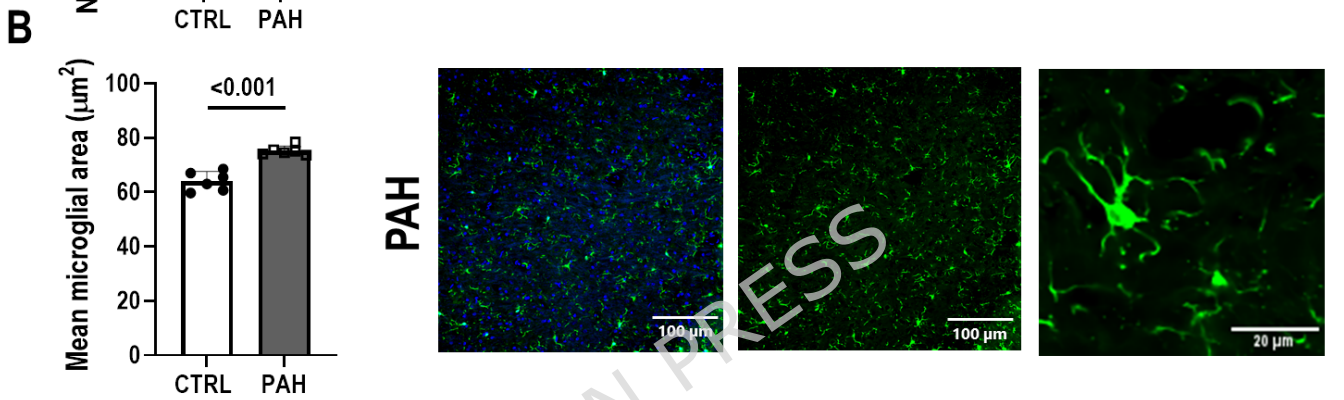
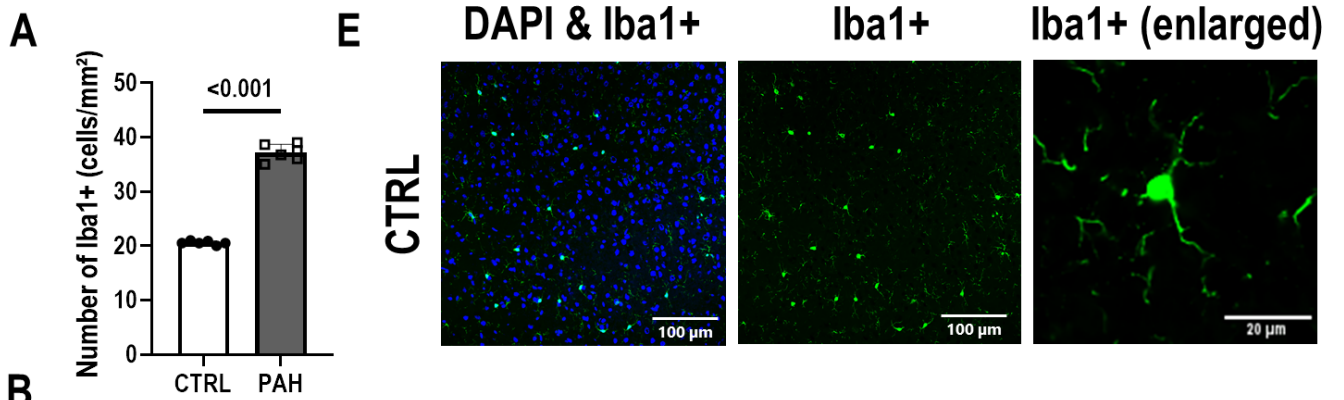
## Microglia

**A** Cortex**B** Hippocampus**C** Cortex**D** Hippocampus**E****F****G****H**

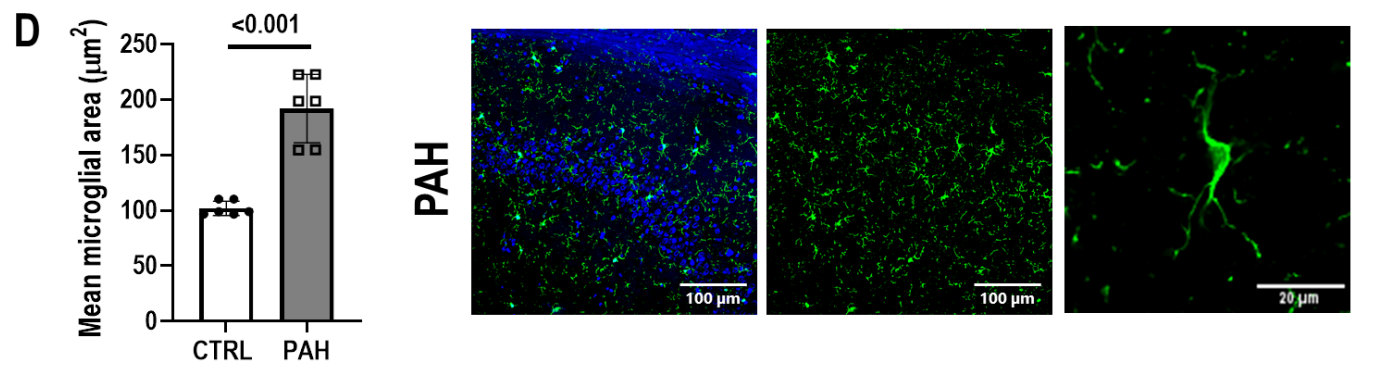
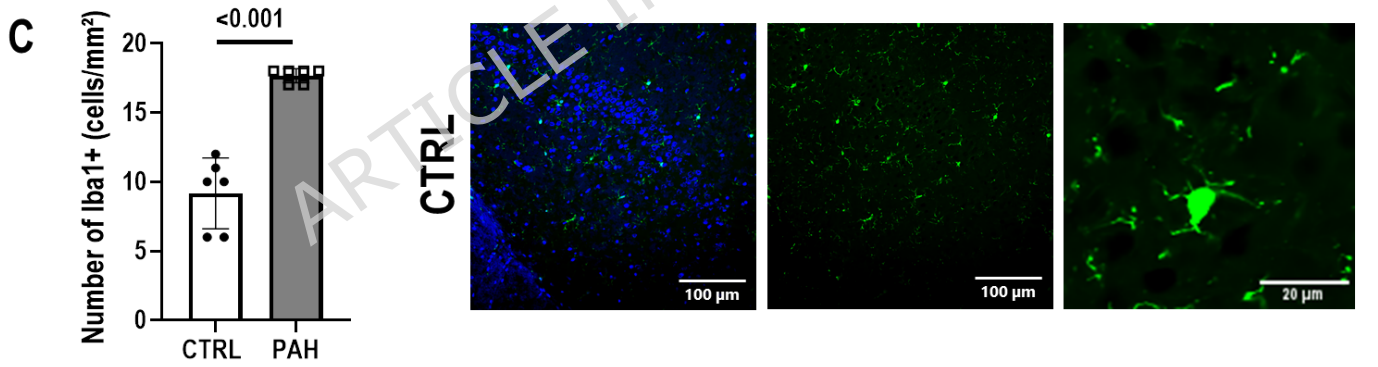




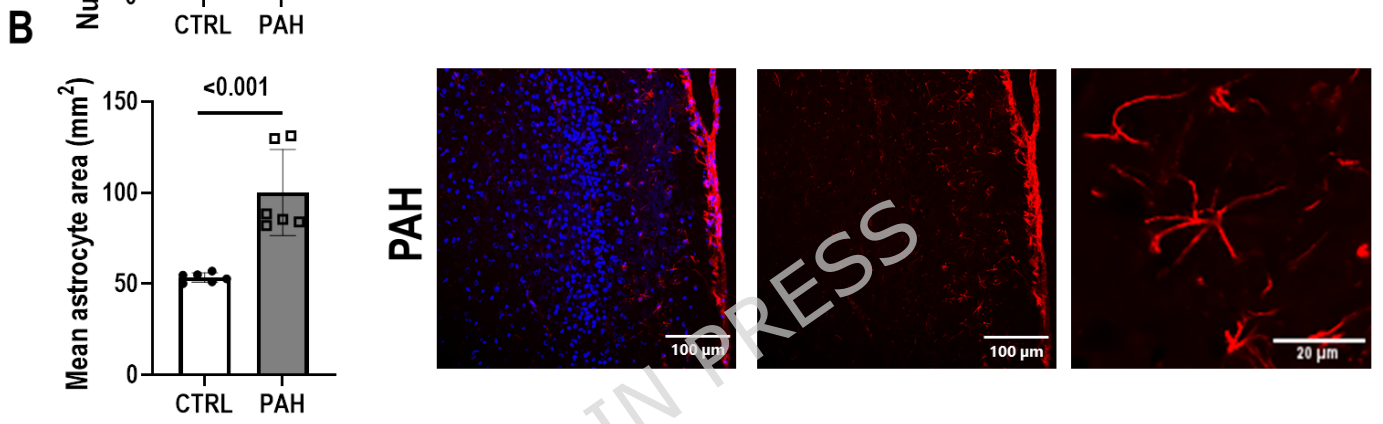
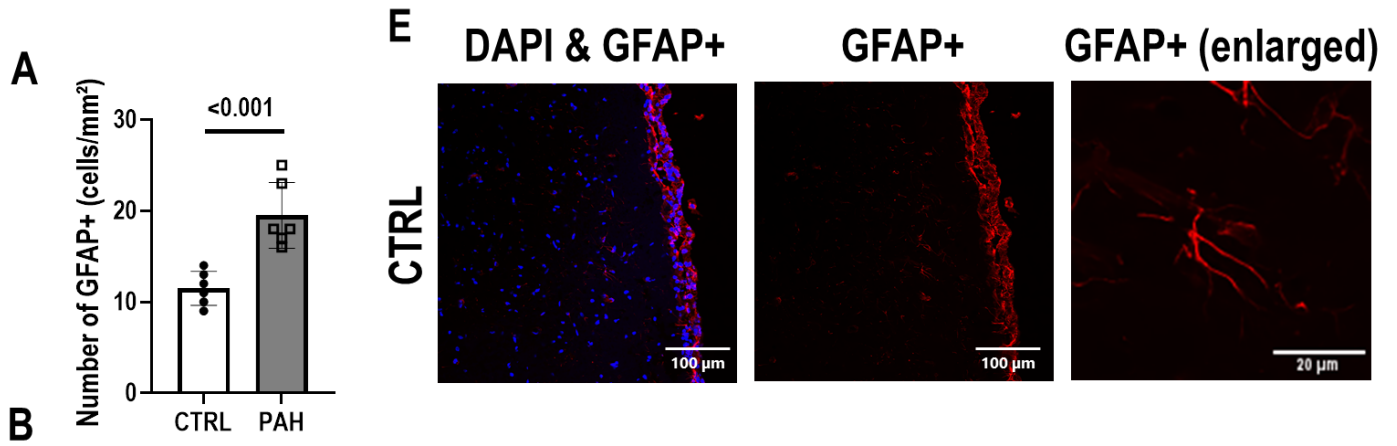
## Cortex



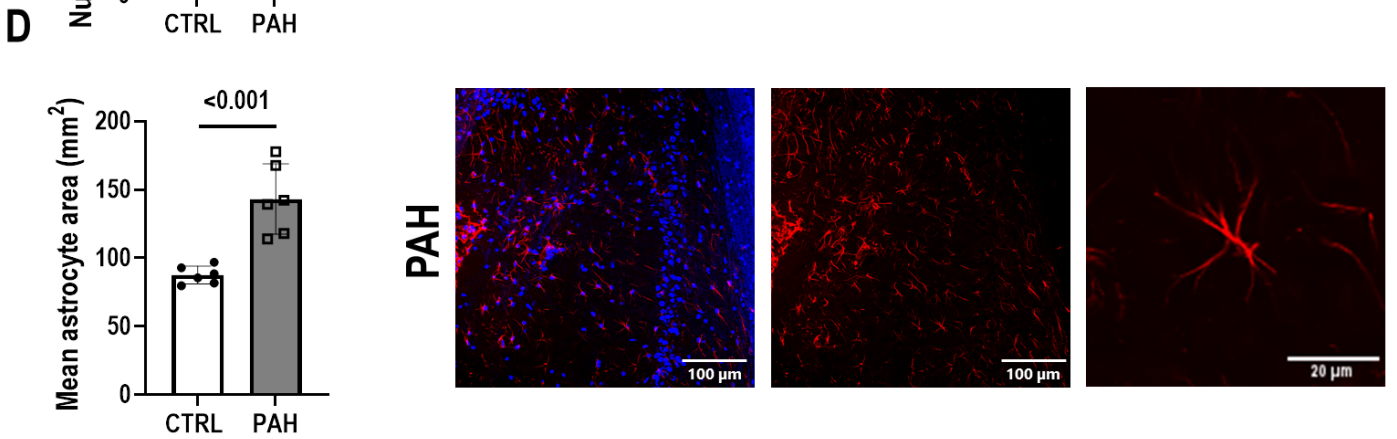
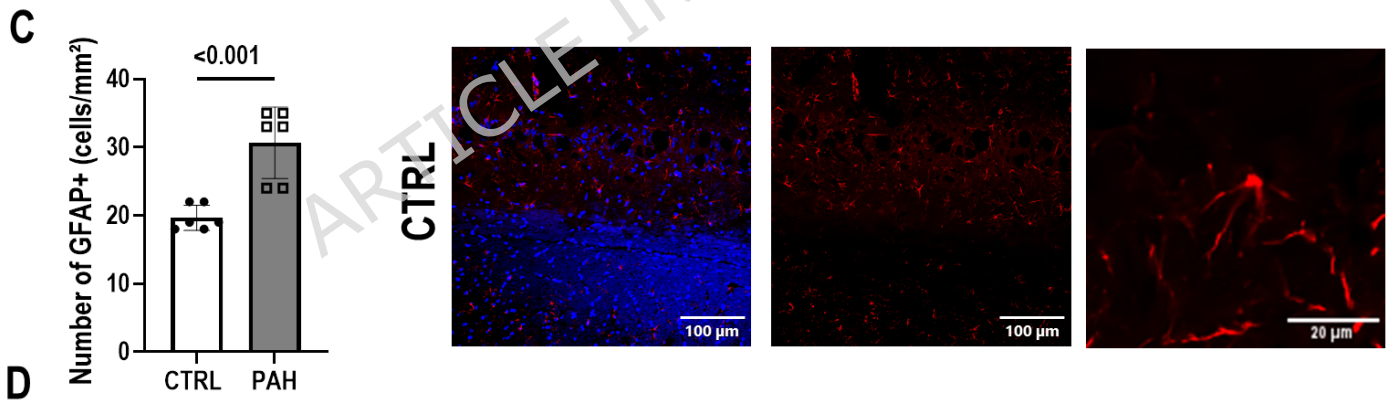
## Hippocampus

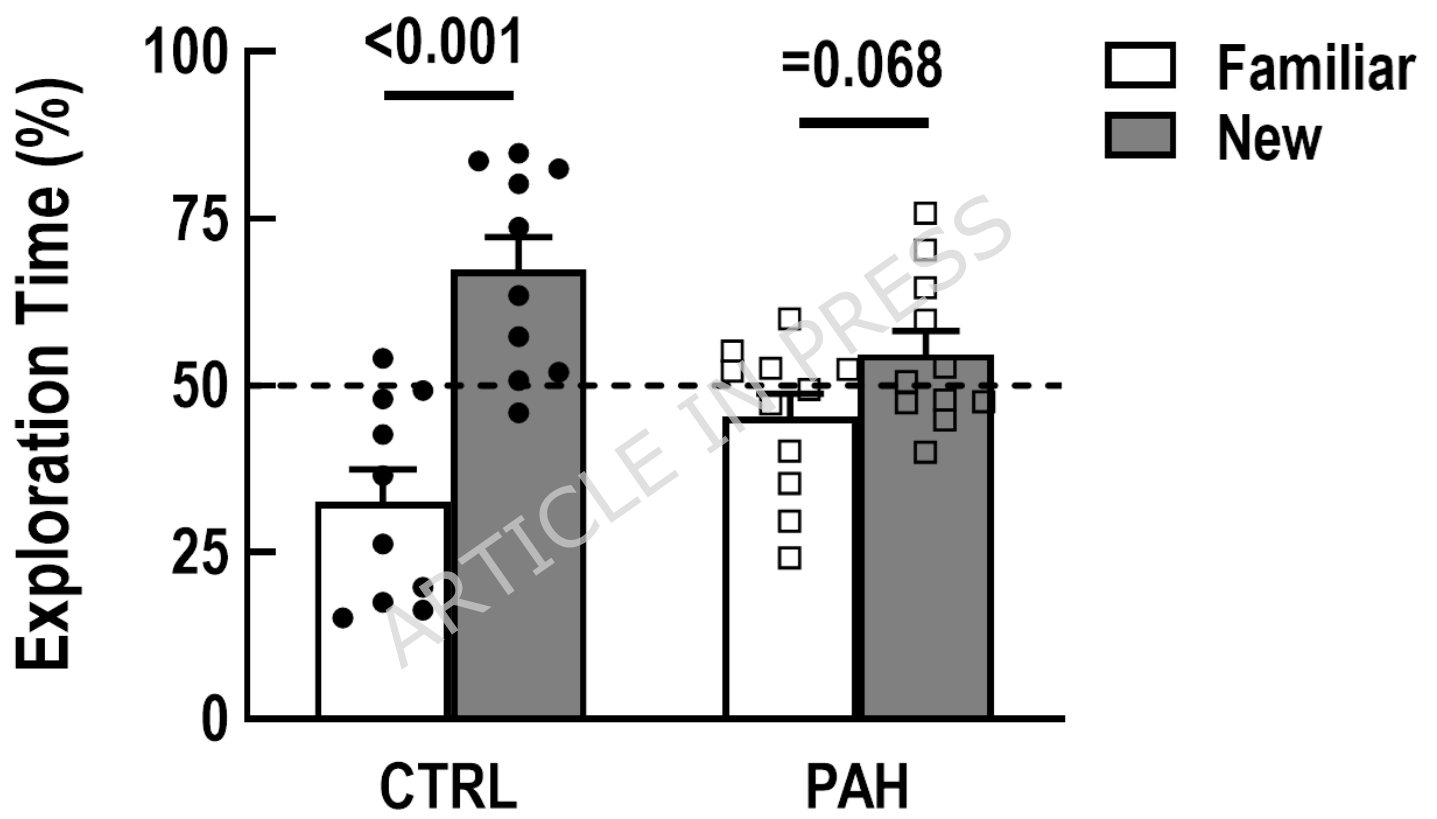


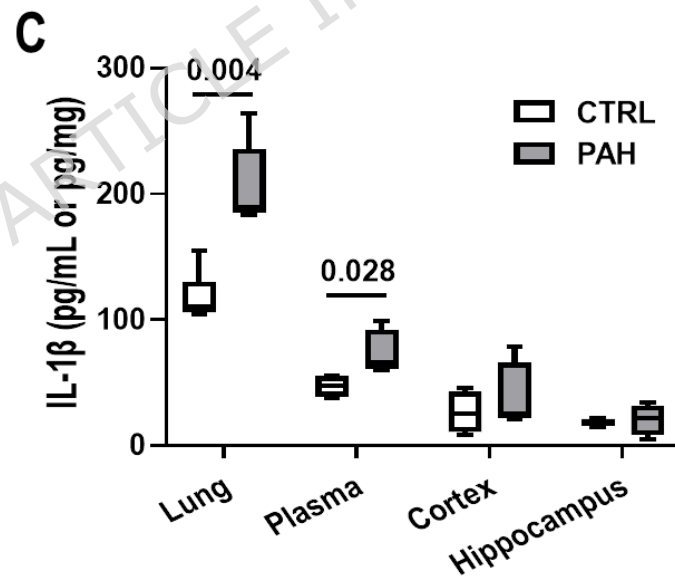
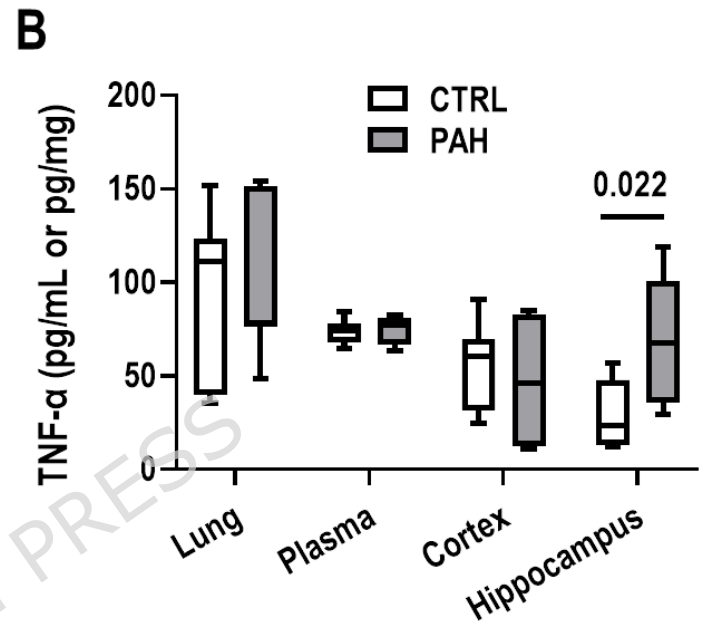
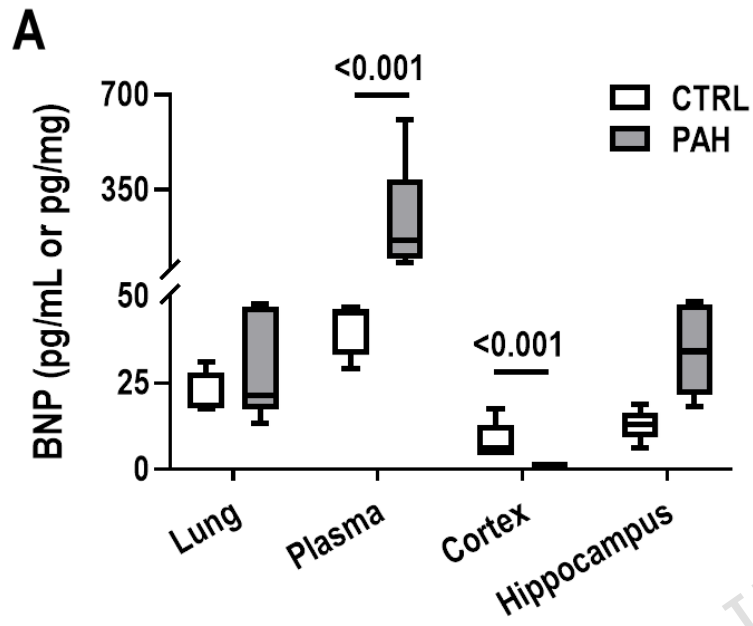
## Cortex



## Hippocampus







Cortex

